A&A 604, L2 (2017)
DOI: 10.1051/0004-6361/201731327

Astronomy & Astrophysics

Letter to the Editor

The complexity of Orion: an ALMA view

II. gGg′-ethylene glycol and acetic acid

C. Favre[1], L. Pagani[2], P. F. Goldsmith[3], E. A. Bergin[4], M. Carvajal[5,6], I. Kleiner[7], G. Melnick[8], and R. Snell[9]

[1] INAF–Osservatorio Astrofisico di Arcetri, Largo E. Fermi 5, Firenze, 50125, Italy
e-mail: cfavre@arcetri.astro.it
[2] LERMA, UMR 8112 du CNRS, Observatoire de Paris, 61 Av. de l'Observatoire, 75014 Paris, France
[3] Jet Propulsion Laboratory, California Institute of Technology, 4800 Oak Grove Drive, Pasadena, CA 91109, USA
[4] Department of Astronomy, University of Michigan, 500 Church Street, Ann Arbor, MI 48109, USA
[5] Dpto. Ciencias Integradas, Unidad GIFMAN-UHU Asociada al CSIC, Universidad de Huelva, 21071 Huelva, Spain
[6] Instituto Universitario Carlos I de Física Teórica y Computacional, Universidad de Granada, Granada, Spain
[7] Laboratoire Interuniversitaire des Systèmes Atmosphériques (LISA), CNRS, UMR 7583, Université de Paris-Est et Paris Diderot, 61, Av. du Général de Gaulle, 94010 Créteil Cedex, France
[8] Harvard-Smithsonian Center for Astrophysics, Cambridge, Massachusetts, USA
[9] Department of Astronomy, University of Massachusetts, Amherst, MA 01003, USA

Received 7 June 2017 / Accepted 5 July 2017

ABSTRACT

We report the first detection and high angular resolution (1.8″ × 1.1″) imaging of acetic acid (CH_3COOH) and gGg′–ethylene glycol ($gGg'(CH_2OH)_2$) toward the Orion Kleinmann–Low (Orion-KL) nebula. The observations were carried out at ∼1.3 mm with ALMA during Cycle 2. A notable result is that the spatial distribution of the acetic acid and ethylene glycol emission differs from that of the other O-bearing molecules within Orion-KL. While the typical emission of O-bearing species harbors a morphology associated with a V-shape linking the hot core region to the compact ridge (with an extension toward the BN object), the emission of acetic acid and ethylene glycol mainly peaks at about 2″ southwest from the hot core region (near sources I and n). We find that the measured CH_3COOH:$aGg'(CH_2OH)_2$ and CH_3COOH:$gGg'(CH_2OH)_2$ ratios differ from those measured toward the low-mass protostar IRAS 16293–2422 by more than one order of magnitude. Our best hypothesis to explain these findings is that CH_3COOH, $aGg'(CH_2OH)_2$, and $gGg'(CH_2OH)_2$ are formed on the icy surface of grains and are then released into the gas-phase via co-desorption with water, by way of a bullet of matter ejected during the explosive event that occurred in the heart of the nebula about 500−700 yr ago.

Key words. astrochemistry – ISM: molecules – radio lines: ISM

1. Introduction

The Orion Kleinmann–Low nebula (hereafter Orion–KL) is the high-mass star-forming region closest to Earth (388 ± 5 pc, Kounkel et al. 2017). Its proximity and rich molecular composition make this region well suited for astrochemical study. In this context, numerous single-dish surveys, including the broadband *Herschel*/HIFI HEXOS survey (Bergin et al. 2010; Crockett et al. 2014), as well as interferometric observations have been performed toward this region (e.g., Favre et al. 2015; Pagani et al. 2017, and references therein). It is important to note that two main molecular components are associated with Orion-KL: the compact ridge, and the hot core. The latter region may have resulted from interaction of the surrounding gas with remnants of the explosive event, triggered by the close encounter of the sources I, n, and the BN object, which occurred in the region about 500–700 yr ago (e.g., see Zapata et al. 2011; Nissen et al. 2012, and references therein). Thus, the complex physical structure and history make Orion-KL an interesting source that may not be representative of other high-mass star forming regions, however, to study the production route (at the icy surface of grains and/or in the gas phase) of complex organic molecules (i.e., molecules that contain six or more atoms, including carbon, hereafter COMs, see Herbst & van Dishoeck 2009). Although present in other star-forming regions, some COMs have not yet been detected in Orion-KL. This is mainly due to sensitivity limitation and a high spectral confusion level (e.g., see Tercero et al. 2010). High resolution and sensitivity, as offered by ALMA, are thus mandatory to search for weak lines associated with COMs. In this context, we have used ALMA during Cycle 2 to perform deep observations of this region in a fraction of band 6 (≈1−2 mm).

Our ALMA Cycle 2 data and first results are given in a companion paper by Pagani et al. (2017, hereafter Paper I). In this Letter, we focus on acetic acid (CH_3COOH) and the gGg′ conformer of ethylene glycol ($gGg'(CH_2OH)_2$) and report their first detection in Orion-KL. The detection of acetic acid in Orion-KL has not yet been reported, although a few transitions may be present in the IRAM 30 m survey by Tercero et al. (2011). However, this species is known to be present in low-mass and high-mass star-forming regions (e.g., Remijan et al. 2003; Shiao et al. 2010; Jørgensen et al. 2016). Regarding gGg′-ethylene glycol, this conformer has only been detected toward the Class 0 protostar IRAS 16293–2422 by Jørgensen et al. (2016). Incidentally, the most stable conformer of ethylene glycol (aGg′) is detected toward low-, intermediate-, and high-mass sources, including Orion-KL (see, e.g., Fuente et al. 2014; Lykke et al. 2015; Brouillet et al. 2015; Rivilla et al. 2017, and references therein). In Sect. 2 we briefly describe our ALMA observations. Results and analysis are given and discussed in Sects. 3 and 4, respectively.

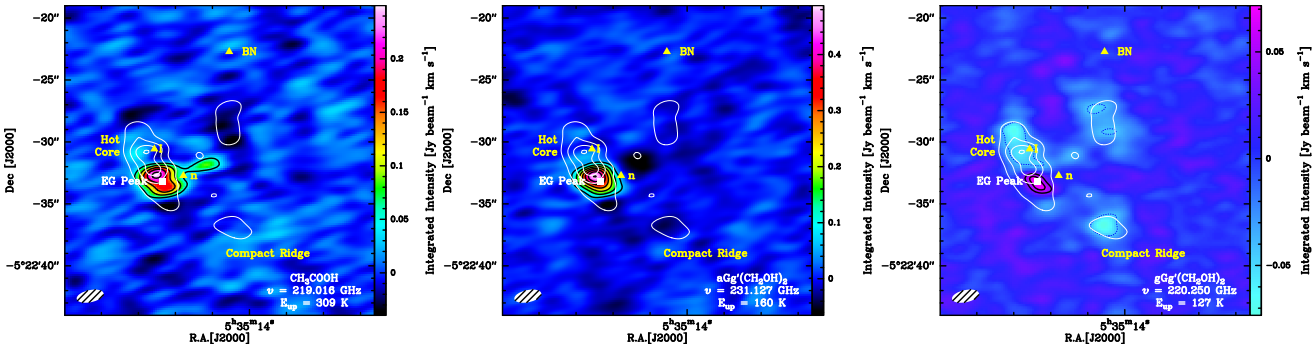

Fig. 1. *Left panel*: CH_3COOH integrated emission map at 219 016 MHz. The first contour and the level step are at 5σ (where $1\sigma = 9.3 \times 10^{-3}$ Jy beam^{-1} km s^{-1}). *Middle panel*: aGg′$(CH_2OH)_2$ integrated emission map at 231 127 MHz. The first contour and the level step are at 5σ (where $1\sigma = 1.4 \times 10^{-2}$ Jy beam^{-1} km s^{-1}). *Right panel*: gGg′$(CH_2OH)_2$ integrated emission map at 220 250 MHz. The contour levels are at -4, 4, and 6σ (where $1\sigma = 1 \times 10^{-2}$ Jy beam^{-1} km s^{-1}). A narrow v_{LSR} interval (from 7 to 9 km s^{-1}) has been selected to reduce confusion by nearby lines (see Sect. 3.3 and Appendix C). Positions of the radio source I, the BN object, and the IR source n (see Goddi et al. 2011) are indicated by yellow triangles. The white square indicates the position of the ethylene glycol peak ($\alpha_{J2000} = 05^h35^m14\overset{s}{.}47$, $\delta_{J2000} = -05°22'33\overset{''}{.}17$) by BD15. Finally, the continuum emission at 235 GHz is overlaid in white contours with a level step of 0.2 Jy beam^{-1} (Paper I).

2. Observations and data reduction

Acetic acid and ethylene glycol lines toward Orion–KL were observed with 37 antennas on 2014 December 29 and with 39 antennas on 2014 December 30. The two following phase-tracking centers were used to perform the observations: $\alpha_{J2000} = 05^h35^m14\overset{s}{.}16$, $\delta_{J2000} = -05°22'31\overset{''}{.}504$ and $\alpha_{J2000} = 05^h35^m13\overset{s}{.}477$, $\delta_{J2000} = -05°22'08\overset{''}{.}50$. The observations lie in the frequency range 215.15 GHz to 252.04 GHz in band 6 and cover about 16 GHz of effective bandwidth with a spectral resolution of about 0.7 km s^{-1}. Data reduction and continuum subtraction were performed through the Common Astronomy Software Applications (CASA) software (McMullin et al. 2007). The cleaning of the spectral lines was performed using the GILDAS software[1]. The resulting synthesized beam is typically $1.8'' \times 1.1''$ (PA of 84°). For further details, see Paper I.

3. Data analysis and results

3.1. Acetic acid and ethylene glycol molecular frequencies

We used the spectroscopic data parameters from Ilyushin et al. (2008) and Ilyushin et al. (2013) for acetic acid, with the following line selection criteria: Einstein spontaneous emission coefficient $A_{ij} \geq 5 \times 10^{-5}$ s^{-1} and upper level energy $E_{up} \leq 400$ K. For the partition function we adopted the complete rotational-torsional-vibrational partition function given by Calcutt, Woods, Carvajal et al. (in prep.).

For the two ethylene glycol conformers we used the spectroscopic data parameters from Christen & Müller (2003) and Müller & Christen (2004) that are available from the Cologne Database for Molecular Spectroscopy catalog (CDMS, Müller et al. 2005). More specifically, we searched for transitions up to $E_{up} \simeq 400$ K, and $A_{ij} \geq 1 \times 10^{-4}$ s^{-1}. The energy difference between the two conformers is about 200 cm^{-1}, the more stable conformer being the aGg′-ethylene glycol (Müller & Christen 2004). Further details about the difference between the aGg′ and the gGg′ conformer can be found in Brouillet et al. (2015, hereafter BD15).

[1] http://www.iram.fr/IRAMFR/GILDAS/

3.2. LTE modeling

Our analysis is based on the assumption that local thermodynamic equilibrium (LTE) is reached. This assumption is reasonable given that LTE modeling of a thousand emissive transitions assigned to simple and complex molecules fits the *Herschel*/HIFI observations performed toward Orion-KL well (see Crockett et al. 2014). In addition, we assume that all the species emit at the same rotational temperature within the same source size. We used the CLASS extension WEEDS (Maret et al. 2011) to model the acetic acid and ethylene glycol (both aGg′ and gGg′ conformer) emission, which we assume to be optically thin. We used the values derived for aGg′$(CH_2OH)_2$ by BD15 as input parameter to initialize our models.

3.3. Emission map

The CH_3COOH, aGg′$(CH_2OH)_2$ and gGg′$(CH_2OH)_2$ emission maps integrated over the line profile are shown in Fig. 1. The nominal velocity of Orion–KL is $v_{LSR} = 7.6$ km s^{-1}. It is important to note that the northwest extension seen in the acetic acid emission map is due to contamination by a U-line (see Appendix C) and is not related to the acetic acid emission. Although we used a restricted v_{LSR} interval to produce the maps, confusion still dominates the region (Paper I).

A salient result is that the distribution of the emission associated with these molecules is similar within the beam, and the main emission peak is located about 2″ southwest of the hot core, near radio source I and the IR source n. This peak corresponds to the ethylene glycol peak (hereafter EGP) identified by BD15 for the aGg′$(CH_2OH)_2$ conformer. An outstanding result is that as for the aGg′$(CH_2OH)_2$ molecule (BD15), the distribution of the emission associated with the acetic acid and the gGg′-ethylene glycol conformer differs from that of typical O-bearing species within Orion-KL. Indeed, the emission of the targeted species appears to come from a compact source in the vicinity of the hot core region, while the emission associated with O-bearing molecules, such as methyl formate (e.g., see Favre et al. 2011, and Appendix D), is generally described by an extended V-shape within Orion-KL that links the hot core component to the compact ridge region and extends toward the BN object (e.g., Guélin et al. 2008).

Table 1. Best-fit line parameters and derived peak column densities for acetic acid and ethylene glycol toward Orion–KL EGP.

Molecule	Component 1				Component 2			
	v (km s^{-1})	$\Delta v_{1/2}$ (km s^{-1})	$T_{\rm rot}$ (K)	N (10^{15} cm^{-2})	v (km s^{-1})	$\Delta v_{1/2}$ (km s^{-1})	$T_{\rm rot}$ (K)	N (10^{15} cm^{-2})
CH_3COOH	7.9	2.5	140	12	5.1	2.3	140	3.3
aGg′$(CH_2OH)_2$	7.8	2.1	140	6.8	5.1	2.1	140	1.5
gGg′$(CH_2OH)_2$	7.8	2.1	140	2.7	5.1	2.1	140	0.66

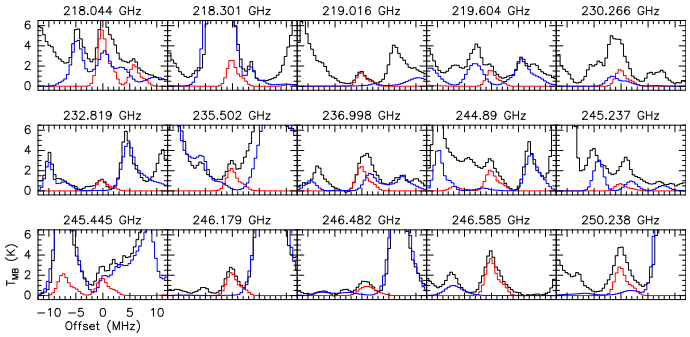

Fig. 2. ALMA observations (black) overlaid with the WEEDS model for acetic acid (red). The sum of the modeled emission from all the other species is overlaid in blue (Paper I).

3.4. Spectra

Spectra of a sample of the most intense transitions (i.e., emitting above the 5σ level) of acetic acid (15 transitions from $E_{\rm up}$ = 70 K up to 318 K, including 5 unblended transitions), aGg′ ethylene glycol (50 transitions from $E_{\rm up}$ = 111 K up to 266 K, including 19 unblended transitions) and gGg′ ethylene glycol (22 transitions from $E_{\rm up}$ = 102 K up to 216 K, including 5 unblended transitions) toward the EGP region are displayed in Figs. 2, 3, and 4, respectively. In addition, our best by-eye WEEDS fits together with the sum of the modeled emission from all the other species in the region (Paper I) are also overlaid in these figures. Tables A.1, A.2, and A.3 in Appendix A list the spectroscopic line parameters for the displayed acetic acid, aGg′–ethylene glycol, and gGg′–ethylene glycol transitions, respectively. The bulk of the emission associated with the targeted molecules peaks at about 7.8–7.9 km s^{-1}. Nonetheless, all the line profiles display an extended blueshifted wing. Thus, two velocity components, one around 8 km s^{-1} and the other at about 5 km s^{-1}, are required to fit the emission. The model parameters that best reproduce the ALMA observations of acetic acid and ethylene glycol (both conformers) in the direction of the EGP region are summarized in Table 1. In the present analysis we assume an overall uncertainty in the range 30%–40%.

3.5. Column densities and relative abundances

Table 1 gives the derived CH_3COOH, aGg′$(CH_2OH)_2$, and gGg′$(CH_2OH)_2$ peak column densities assuming a source size of 3″ for each velocity component. We note that our best aGg′$(CH_2OH)_2$ fit result (v, Δ_v, $T_{\rm rot}$ and N) is consistent within the uncertainties (~30%–40%) with the value reported by BD15.

Table B.1 lists the relative abundance ratios for acetic acid and ethylene glycol derived from our best model results (see Table 1) toward the two velocity components observed in direction of the EGP peak. The derived abundance ratios are equal within the error bars for both velocity components. It is important to note that BD15 reported an upper limit on

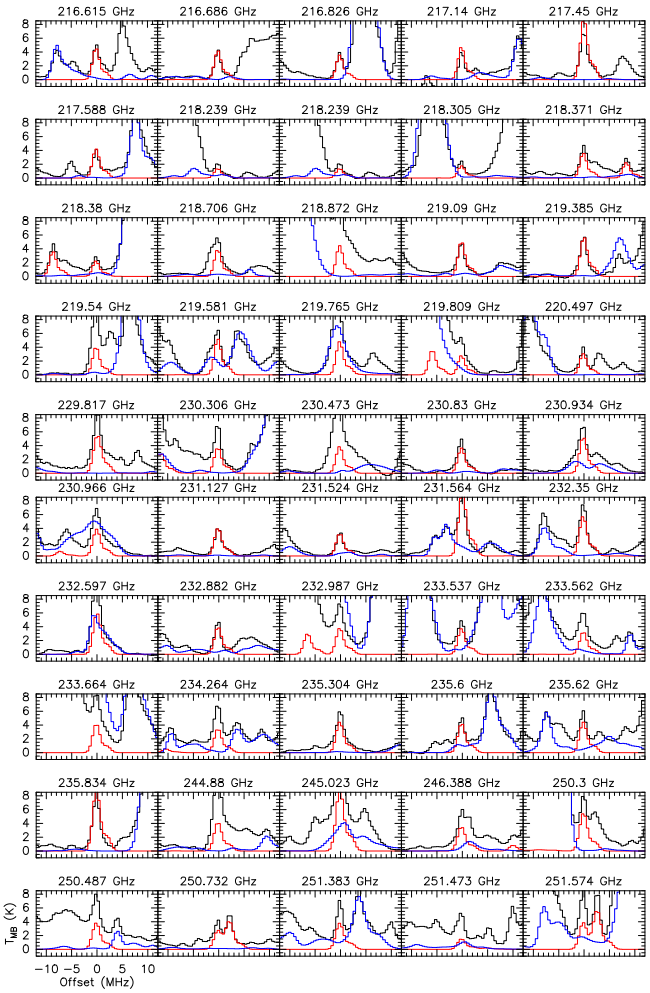

Fig. 3. ALMA observations (black) overlaid with the WEEDS model for aGg′ ethylene glycol (red). The sum of the modeled emission from all the other species is overlaid in blue (Paper I).

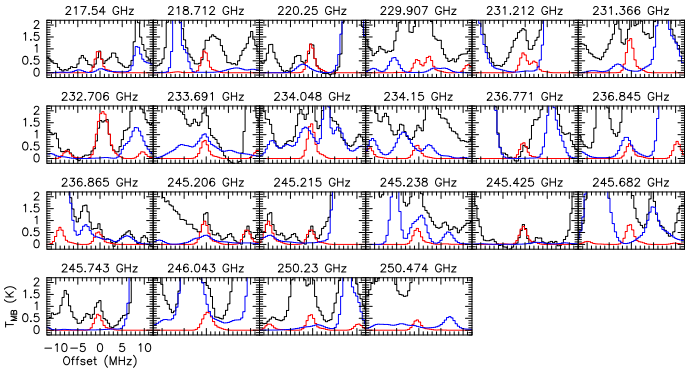

Fig. 4. ALMA observations (black) overlaid with the WEEDS model for gGg′ ethylene glycol (red). The sum of the modeled emission from all the other species is overlaid in blue (Paper I).

the aGg′$(CH_2OH)_2$/gGg′$(CH_2OH)_2$ ratio of 5. This discrepancy apparently results from an underestimate of the limit on the gGg′$(CH_2OH)_2$ column density by BD15.

4. Discussion

In Fig. 5 we show the relative abundance ratios, CH_3COOH:aGg′$(CH_2OH)_2$:gGg′$(CH_2OH)_2$, derived in this study along with those derived toward the low-mass protostar IRAS 16293–2422 by Jørgensen et al. (2016). It is immediately apparent that the CH_3COOH:$(CH_2OH)_2$ ratios measured in the direction of Orion-KL are higher than those of the low-mass protostar IRAS 16293–2422 by over an order of magnitude. We also note that the aGg′$(CH_2OH)_2$:gGg′$(CH_2OH)_2$ ratio seems to be, within the error bars, the same for both regions. The fact that Jørgensen et al. (2016) assumed different rotational temperatures for the two conformers to estimate this ratio might explain the slight difference. Lykke et al. (2015) have shown that the source luminosities are likely correlated with relative abundances of complex organic molecules. These findings lead to the question whether and how the physical conditions in these regions, in particular Orion-KL, affect the production and the possible release to the gas-phase of these species.

Both CH_3COOH and $(CH_2OH)_2$ are believed to mainly be formed on the icy surface of grains, although gas-phase formation routes cannot be ruled out (see, e.g., Laas et al. 2011; Rivilla et al. 2017). Interestingly enough, Garrod et al. (2008) have shown that ethylene glycol in grain mantles is produced more efficiently than acetic acid by at least one order of magnitude. This naturally explains the observation that the abundance ratio $CH_3COOH/(CH_2OH)_2$ is lower in low-mass star-forming regions. However, regarding Orion-KL, an additional mechanism is required to explain the overabundance of CH_3COOH. It is noteworthy that Wright & Plambeck (2017) have recently proposed that a bullet of matter ejected during the explosive event that occurred ~500−700 yr ago (Nissen et al. 2012) has impacted the EGP region. More specifically, using high angular resolution ALMA observations, Wright & Plambeck (2017) have reported a molecular ring in HC_3N, HCN, and SO_2 that is not associated with continuum emission. In this context, it is important to note that the distribution of acetic acid and ethylene glycol is cospatial with this ring (Fig. E.1). In addition, both acetic acid and ethylene glycol line profiles present a blueshifted emission wing (i.e., the 5 km s^{-1} velocity component), this specific asymmetric line profile being also observed for other molecules in this region (e.g., methanol and formic acid, Paper I). These findings strongly suggest that this region is peculiar and is different from other star-forming regions. The impact that took place here has led to the release of icy COMs in the gas phase, generating the observed gas motions together with a rich molecular composition that may reflect gas-phase chemistry in an induced shock or post-shock stage.

Acknowledgements. CF acknowledges support from the Italian Ministry of Education, Universities and Research, project SIR (RBSI14ZRHR). The authors thank Hannah Calcutt for providing the acetic acid partition function. We also thank Melvyn Wright and Rick Plambeck for their HC_3N emission map. This work was carried out in part at the Jet Propulsion Laboratory, which is operated for NASA by the California Institute of Technology. MC acknowledges financial funding from the project FIS2014-53448-C2-2-P (MINECO, Spain), and CMST COST Action CM1405 MOLIM. CF and MC acknowledge support from CMST COST Action CM1401 Our Astro-Chemical History. LP thanks Arnaud Belloche and H.S.P. Müller for their help with molecular spectroscopy data. CF thanks Claudio Codella for an enlightening discussion on shocks. Finally, CF thanks Vianney Taquet and Franck Hersant for a fruitful discussion about the binding energies and acetic acid formation routes. This paper makes use of the following ALMA data: ADS/JAO.ALMA#2013.1.00533.S. ALMA is a partnership of ESO (representing its member states), NSF (USA) and NINS (Japan), together with NRC (Canada), NSC and ASIAA (Taiwan), and KASI (Republic of Korea), in cooperation with the Republic of Chile. The Joint ALMA Observatory is operated by ESO, AUI/NRAO and NAOJ.

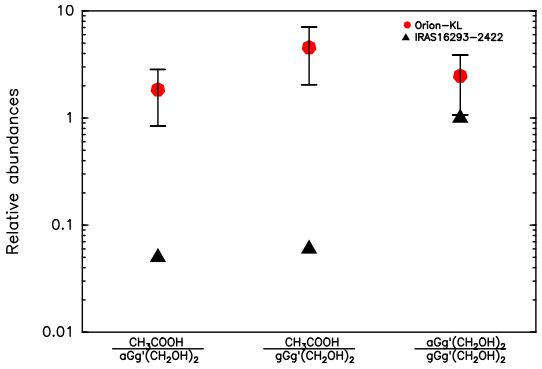

Fig. 5. Acetic acid and ethylene glycol abundance ratios toward Orion-KL (red circles, this study) and IRAS 16293−2422 (black triangles, Jørgensen et al. 2016). The ratios for Orion-KL are obtained from the sum of the velocity components given in Table 1.

References

Bergin, E. A., Phillips, T. G., Comito, C., et al. 2010, A&A, 521, L20
Brouillet, N., Despois, D., Lu, X.-H., et al. 2015, A&A, 576, A129
Christen, D., & Müller, H. S. P. 2003, Physical Chemistry Chemical Physics (Incorporating Faraday Transactions), 5, 3600
Crockett, N. R., Bergin, E. A., Neill, J. L., et al. 2014, ApJ, 787, 112
Favre, C., Bergin, E. A., Neill, J. L., et al. 2015, ApJ, 808, 155
Favre, C., Despois, D., Brouillet, N., et al. 2011, A&A, 532, A32
Fuente, A., Cernicharo, J., Caselli, P., et al. 2014, A&A, 568, A65
Garrod, R. T., Weaver, S. L. W., & Herbst, E. 2008, ApJ, 682, 283
Goddi, C., Humphreys, E. M. L., Greenhill, L. J., Chandler, C. J., & Matthews, L. D. 2011, ApJ, 728, 15
Guélin, M., Brouillet, N., Cernicharo, J., Combes, F., & Wooten, A. 2008, Ap&SS, 313, 45
Herbst, E., & van Dishoeck, E. F. 2009, ARA&A, 47, 427
Ilyushin, V., Kleiner, I., & Lovas, F. J. 2008, J. Phys. Chem. Ref. Data, 37, 97
Ilyushin, V. V., Endres, C. P., Lewen, F., Schlemmer, S., & Drouin, B. J. 2013, J. Mol. Spectr., 290, 31
Jørgensen, J. K., van der Wiel, M. H. D., Coutens, A., et al. 2016, A&A, 595, A117
Kounkel, M., Hartmann, L., Loinard, L., et al. 2017, ApJ, 834, 142
Laas, J. C., Garrod, R. T., Herbst, E., & Widicus Weaver, S. L. 2011, ApJ, 728, 71
Lykke, J. M., Favre, C., Bergin, E. A., & Jørgensen, J. K. 2015, A&A, 582, A64
Maret, S., Hily-Blant, P., Pety, J., Bardeau, S., & Reynier, E. 2011, A&A, 526, A47
McMullin, J. P., Waters, B., Schiebel, D., Young, W., & Golap, K. 2007, in Astronomical Data Analysis Software and Systems XVI, eds. R. A. Shaw, F. Hill, & D. J. Bell, ASP Conf. Ser., 376, 127
Müller, H. S. P., & Christen, D. 2004, J. Mol. Spectr., 228, 298
Müller, H. S. P., Schlöder, F., Stutzki, J., & Winnewisser, G. 2005, J. Mol. Struct., 742, 215
Nissen, H. D., Cunningham, N. J., Gustafsson, M., et al. 2012, A&A, 540, A119
Pagani, L., Favre, C., Goldsmith, P. F., et al. 2017, A&A, 604, A32
Remijan, A., Snyder, L. E., Friedel, D. N., Liu, S., & Shah, R. Y. 2003, ApJ, 590, 314
Rivilla, V. M., Beltrán, M. T., Cesaroni, R., et al. 2017, A&A, 598, A59
Shiao, Y., Looney, L. W., Remijan, A. J., Snyder, L. E., & Friedel, D. N. 2010, ApJ, 716, 286
Tercero, B., Cernicharo, J., Pardo, J. R., & Goicoechea, J. R. 2010, A&A, 517, A96
Tercero, B., Vincent, L., Cernicharo, J., Viti, S., & Marcelino, N. 2011, A&A, 528, A26
Wright, M. C. H., & Plambeck, R. L. 2017, ApJ, 843, 83
Zapata, L. A., Schmid-Burgk, J., & Menten, K. M. 2011, A&A, 529, A24

Appendix A: Spectroscopic line parameters

Tables A.1–A.3 list the spectroscopic line parameters for the acetic acid, aGg′–ethylene glycol, and gGg′–ethylene glycol lines that are displayed in Figs. 2–4, respectively.

Table A.1. Spectroscopic data of the acetic acid lines displayed in Fig. 2

Frequency (MHz)	Symmetry	Quantum number J_{K_a,K_c}, v_t(up)	Quantum number J_{K_a,K_c},v_t(low)	$A_{u,l}$ (s^{-1})	g_{up}	E_{up} (K)
218 044.2146	A	$20_{(0,20)}, v_t = 0$	$19_{(1,19)}, v_t = 0$	2.25e-05	82	112.2
218 044.2146	A	$20_{(1,20)}, v_t = 0$	$19_{(0,19)}, v_t = 0$	2.25e-05	82	112.2
218 044.2146	A	$20_{(0,20)}, v_t = 0$	$19_{(0,19)}, v_t = 0$	6.06e-05	82	112.2
218 044.2146	A	$20_{(1,20)}, v_t = 0$	$19_{(1,19)}, v_t = 0$	6.06e-05	82	112.2
218 301.0685	E	$20_{(0,20)}, v_t = 1$	$19_{(0,19)}, v_t = 1$	2.44e-08	82	217.4
218 301.0685	E	$20_{(1,20)}, v_t = 1$	$19_{(1,19)}, v_t = 1$	2.44e-08	82	217.4
218 301.0685	E	$20_{(0,20)}, v_t = 1$	$19_{(1,19)}, v_t = 1$	8.31e-05	82	217.4
218 301.0685	E	$20_{(1,20)}, v_t = 1$	$19_{(0,19)}, v_t = 1$	8.31e-05	82	217.4
219 016.0364	E	$20_{(0,20)}, v_t = 2$	$19_{(1,19)}, v_t = 2$	6.41e-05	82	309.0
219 016.0365	E	$20_{(0,20)}, v_t = 2$	$19_{(0,19)}, v_t = 2$	1.77e-05	82	309.0
219 016.0385	E	$20_{(1,20)}, v_t = 2$	$19_{(1,19)}, v_t = 2$	1.77e-05	82	309.0
219 016.0386	E	$20_{(1,20)}, v_t = 2$	$19_{(0,19)}, v_t = 2$	6.41e-05	82	309.0
219 603.9437	A	$20_{(0,20)}, v_t = 2$	$19_{(1,19)}, v_t = 2$	6.51e-06	82	289.1
219 603.9437	A	$20_{(1,20)}, v_t = 2$	$19_{(1,19)}, v_t = 2$	7.77e-05	82	289.1
219 603.9446	A	$20_{(1,20)}, v_t = 2$	$19_{(0,19)}, v_t = 2$	6.51e-06	82	289.1
219 603.9446	A	$20_{(0,20)}, v_t = 2$	$19_{(0,19)}, v_t = 2$	7.77e-05	82	289.1
230 266.0061	A	$21_{(0,21)}, v_t = 2$	$20_{(1,20)}, v_t = 2$	2.71e-05	86	300.2
230 266.0061	A	$21_{(1,21)}, v_t = 2$	$20_{(0,20)}, v_t = 2$	2.71e-05	86	300.2
230 266.0061	A	$21_{(0,21)}, v_t = 2$	$20_{(0,20)}, v_t = 2$	7.02e-05	86	300.2
230 266.0061	A	$21_{(1,21)}, v_t = 2$	$20_{(1,20)}, v_t = 2$	7.02e-05	86	300.2
232 818.7007	E	$19_{(2,17)}, v_t = 2$	$18_{(3,16)}, v_t = 2$	7.31e-05	78	317.7
232 818.7077	E	$19_{(3,17)}, v_t = 2$	$18_{(3,16)}, v_t = 2$	1.06e-05	78	317.7
232 818.7318	E	$19_{(2,17)}, v_t = 2$	$18_{(2,16)}, v_t = 2$	1.06e-05	78	317.7
232 818.7388	E	$19_{(3,17)}, v_t = 2$	$18_{(2,16)}, v_t = 2$	7.31e-05	78	317.7
235 501.6832	A	$20_{(2,18)}, v_t = 1$	$19_{(3,17)}, v_t = 1$	3.21e-05	82	241.5
235 501.6832	A	$20_{(3,18)}, v_t = 1$	$19_{(2,17)}, v_t = 1$	3.21e-05	82	241.5
235 501.6832	A	$20_{(2,18)}, v_t = 1$	$19_{(2,17)}, v_t = 1$	6.14e-05	82	241.5
235 501.6832	A	$20_{(3,18)}, v_t = 1$	$19_{(3,17)}, v_t = 1$	6.14e-05	82	241.5
236 998.1508	A	$21_{(1,20)}, v_t = 1$	$20_{(1,19)}, v_t = 1$	1.01e-04	86	245.0
236 998.1508	A	$21_{(2,20)}, v_t = 1$	$20_{(2,19)}, v_t = 1$	1.01e-04	86	245.0
236 998.1508	A	$21_{(1,20)}, v_t = 1$	$20_{(2,19)}, v_t = 1$	1.42e-07	86	245.0
236 998.1508	A	$21_{(2,20)}, v_t = 1$	$20_{(1,19)}, v_t = 1$	1.42e-07	86	245.0
244 889.6209	A	$20_{(3,17)}, v_t = 1$	$19_{(3,16)}, v_t = 1$	2.42e-05	82	249.1
244 889.6209	A	$20_{(4,17)}, v_t = 1$	$19_{(4,16)}, v_t = 1$	2.42e-05	82	249.1
244 889.6209	A	$20_{(3,17)}, v_t = 1$	$19_{(4,16)}, v_t = 1$	7.48e-05	82	249.1
244 889.6209	A	$20_{(4,17)}, v_t = 1$	$19_{(3,16)}, v_t = 1$	7.48e-05	82	249.1
245 237.0813	A	$12_{(11,1)}, v_t = 1$	$11_{(10,2)}, v_t = 1$	7.14e-05	50	187.2
245 444.9402	E	$11_{(11,1)}, v_t = 0$	$10_{(10,1)}, v_t = 0$	8.23e-05	46	70.1
246 179.2041	A	$21_{(2,19)}, v_t = 1$	$20_{(3,18)}, v_t = 1$	3.88e-05	86	253.3
246 179.2041	A	$21_{(3,19)}, v_t = 1$	$20_{(2,18)}, v_t = 1$	3.88e-05	86	253.3
246 179.2041	A	$21_{(2,19)}, v_t = 1$	$20_{(2,18)}, v_t = 1$	6.89e-05	86	253.3
246 179.2041	A	$21_{(3,19)}, v_t = 1$	$20_{(3,18)}, v_t = 1$	6.89e-05	86	253.3
246 481.9960	A	$19_{(3,16)}, v_t = 2$	$18_{(4,15)}, v_t = 2$	6.01e-05	78	309.9
246 584.8477	E	$18_{(5,13)}, v_t = 0$	$17_{(6,12)}, v_t = 0$	6.11e-05	74	129.1
246 584.8511	E	$18_{(6,13)}, v_t = 0$	$17_{(6,12)}, v_t = 0$	2.23e-05	74	129.1
246 584.8724	E	$18_{(5,13)}, v_t = 0$	$17_{(5,12)}, v_t = 0$	2.23e-05	74	129.1
246 584.8759	E	$18_{(6,13)}, v_t = 0$	$17_{(5,12)}, v_t = 0$	6.11e-05	74	129.1
250 237.9675	E	$23_{(0,23)}, v_t = 1$	$22_{(0,22)}, v_t = 1$	1.11e-04	94	251.9
250 237.9675	E	$23_{(1,23)}, v_t = 1$	$22_{(1,22)}, v_t = 1$	1.11e-04	94	251.9
250 237.9675	E	$23_{(0,23)}, v_t = 1$	$22_{(1,22)}, v_t = 1$	1.54e-05	94	251.9
250 237.9675	E	$23_{(1,23)}, v_t = 1$	$22_{(0,22)}, v_t = 1$	1.54e-05	94	251.9

Table A.2. Spectroscopic data of the aGg' ethylene glycol lines displayed in Fig. 3.

Frequency (MHz)	Quantum number[a] J_{K_a,K_c},v(up)	J_{K_a,K_c},v(low)	$A_{u,l}$ s^{-1}	g_{up}	E_{up} (K)
216 614.952	$20_{(3,17)}, v = 1$	$19_{(3,16)}, v = 0$	2.222E-04	369	110.8
216 685.815	$21_{(3,19)}, v = 1$	$20_{(3,18)}, v = 0$	2.030E-04	387	117.3
216 826.112	$20_{(5,15)}, v = 1$	$19_{(5,14)}, v = 0$	1.792E-04	369	116.8
217 139.723	$21_{(4,17)}, v = 0$	$20_{(4,16)}, v = 1$	2.423E-04	387	123.9
217 449.995	$24_{(1,24)}, v = 0$	$23_{(1,23)}, v = 1$	2.520E-04	441	136.4
217 450.270	$24_{(0,24)}, v = 0$	$23_{(0,23)}, v = 1$	2.520E-04	343	136.4
217 587.548	$21_{(2,19)}, v = 1$	$20_{(2,18)}, v = 0$	2.654E-04	301	117.2
218 238.988	$22_{(17,5)}, v = 0$	$21_{(17,4)}, v = 1$	1.018E-04	315	266.2
218 238.988	$22_{(17,6)}, v = 0$	$21_{(17,5)}, v = 1$	1.018E-04	405	266.2
218 304.671	$22_{(16,6)}, v = 0$	$21_{(16,5)}, v = 1$	1.192E-04	315	250.0
218 304.671	$22_{(16,7)}, v = 0$	$21_{(16,6)}, v = 1$	1.192E-04	405	250.0
218 371.495	$22_{(4,19)}, v = 0$	$21_{(4,18)}, v = 1$	1.881E-04	405	132.6
218 379.983	$22_{(15,7)}, v = 0$	$21_{(15,6)}, v = 1$	1.355E-04	315	234.8
218 379.983	$22_{(15,8)}, v = 0$	$21_{(15,7)}, v = 1$	1.355E-04	405	234.8
218 705.810	$22_{(12,10)}, v = 0$	$21_{(12,9)}, v = 1$	1.786E-04	315	195.1
218 705.810	$22_{(12,11)}, v = 0$	$21_{(12,10)}, v = 1$	1.786E-04	405	195.1
218 872.112	$22_{(11,12)}, v = 0$	$21_{(11,11)}, v = 1$	1.911E-04	405	183.8
218 872.112	$22_{(11,11)}, v = 0$	$21_{(11,10)}, v = 1$	1.911E-04	315	183.8
219 089.720	$22_{(10,13)}, v = 0$	$21_{(10,12)}, v = 1$	2.027E-04	405	173.5
219 089.728	$22_{(10,12)}, v = 0$	$21_{(10,11)}, v = 1$	2.027E-04	315	173.5
219 385.178	$22_{(9,14)}, v = 0$	$21_{(9,13)}, v = 1$	2.136E-04	405	164.3
219 385.426	$22_{(9,13)}, v = 0$	$21_{(9,12)}, v = 1$	2.136E-04	315	164.3
219 540.443	$22_{(2,21)}, v = 1$	$21_{(2,20)}, v = 0$	2.539E-04	315	122.1
219 580.672	$22_{(1,21)}, v = 1$	$21_{(1,20)}, v = 0$	2.568E-04	405	122.0
219 764.926	$20_{(4,16)}, v = 1$	$19_{(4,15)}, v = 0$	2.454E-04	369	113.5
219 809.406	$22_{(8,14)}, v = 0$	$21_{(8,13)}, v = 1$	2.238E-04	315	156.0
220 496.592	$22_{(7,15)}, v = 0$	$21_{(7,14)}, v = 1$	2.339E-04	315	148.8
229 816.573	$23_{(9,15)}, v = 0$	$22_{(9,14)}, v = 1$	2.499E-04	329	175.6
229 817.111	$23_{(9,14)}, v = 0$	$22_{(9,13)}, v = 1$	2.499E-04	423	175.6
230 305.630	$23_{(8,15)}, v = 0$	$22_{(8,14)}, v = 1$	2.610E-04	423	167.4
230 472.528	$21_{(4,17)}, v = 1$	$20_{(4,16)}, v = 0$	2.836E-04	301	124.2
230 830.319	$24_{(2,22)}, v = 0$	$23_{(2,21)}, v = 1$	2.822E-04	343	149.8
230 933.676	$23_{(3,20)}, v = 0$	$22_{(3,19)}, v = 1$	3.166E-04	423	143.3
230 965.547	$23_{(7,17)}, v = 0$	$22_{(7,16)}, v = 1$	2.715E-04	329	160.2
231 127.401	$23_{(7,16)}, v = 0$	$22_{(7,15)}, v = 1$	2.722E-04	423	160.2
231 524.033	$23_{(6,18)}, v = 0$	$22_{(6,17)}, v = 1$	2.714E-04	329	154.1
231 564.005	$24_{(1,24)}, v = 1$	$23_{(1,23)}, v = 0$	3.043E-04	343	136.8
231 564.320	$24_{(0,24)}, v = 1$	$23_{(0,23)}, v = 0$	3.043E-04	441	136.8
232 350.059	$22_{(10,13)}, v = 1$	$21_{(10,12)}, v = 0$	2.420E-04	315	173.8
232 350.068	$22_{(10,12)}, v = 1$	$21_{(10,11)}, v = 0$	2.420E-04	405	173.8
232 597.215	$22_{(9,14)}, v = 1$	$21_{(9,13)}, v = 0$	2.549E-04	315	164.6
232 597.490	$22_{(9,13)}, v = 1$	$21_{(9,12)}, v = 0$	2.548E-04	405	164.6
232 881.533	$23_{(6,17)}, v = 0$	$22_{(6,16)}, v = 1$	2.607E-04	423	154.3
232 987.353	$22_{(8,14)}, v = 1$	$21_{(8,13)}, v = 0$	2.669E-04	405	156.3
233 536.696	$22_{(5,18)}, v = 1$	$21_{(5,17)}, v = 0$	2.930E-04	315	137.7
233 561.785	$22_{(7,16)}, v = 1$	$21_{(7,15)}, v = 0$	2.785E-04	315	149.1
233 664.319	$22_{(7,15)}, v = 1$	$21_{(7,14)}, v = 0$	2.788E-04	405	149.1
234 264.446	$22_{(6,17)}, v = 1$	$21_{(6,16)}, v = 0$	2.839E-04	315	143.0
235 304.050	$22_{(6,16)}, v = 1$	$21_{(6,15)}, v = 0$	2.897E-04	405	143.1
235 600.179	$23_{(2,21)}, v = 1$	$22_{(2,20)}, v = 0$	3.276E-04	329	138.7
235 620.372	$24_{(4,21)}, v = 0$	$23_{(4,20)}, v = 1$	2.881E-04	441	155.4
235 834.240	$26_{(1,26)}, v = 0$	$25_{(1,25)}, v = 1$	3.222E-04	477	159.3
235 834.327	$26_{(0,26)}, v = 0$	$25_{(0,25)}, v = 1$	3.221E-04	371	159.3

Notes. [(a)] Tunnelling is observed between two equivalent equilibrium configurations and splits each rotational level into two distinct states designated as $v = 0$ and $v = 1$ (BD15).

Table A.2. continued.

Frequency (MHz)	Quantum number[a] J_{K_a,K_c},v(up)	J_{K_a,K_c},v(low)	$A_{u,l}$ s^{-1}	g_{up}	E_{up} (K)
244 879.919	$23_{(6,18)}, v = 1$	$22_{(6,17)}, v = 0$	3.028E-04	423	154.4
245 022.738	$27_{(1,27)}, v = 0$	$26_{(1,26)}, v = 1$	3.616E-04	385	171.4
245 022.787	$27_{(0,27)}, v = 0$	$26_{(0,26)}, v = 1$	3.617E-04	495	171.4
246 387.881	$23_{(6,17)}, v = 1$	$22_{(6,16)}, v = 0$	3.280E-04	329	154.6
250 300.410	$25_{(10,16)}, v = 0$	$24_{(10,15)}, v = 1$	3.208E-04	357	209.0
250 300.508	$25_{(10,15)}, v = 0$	$24_{(10,14)}, v = 1$	3.209E-04	459	209.0
250 487.421	$23_{(5,18)}, v = 1$	$22_{(5,17)}, v = 0$	3.606E-04	329	150.3
250 731.885	$25_{(9,17)}, v = 0$	$24_{(9,16)}, v = 1$	3.341E-04	357	199.8
250 734.147	$25_{(9,16)}, v = 0$	$24_{(9,15)}, v = 1$	3.341E-04	459	199.8
251 382.563	$25_{(8,17)}, v = 0$	$24_{(8,16)}, v = 1$	3.471E-04	459	191.6
251 473.045	$25_{(6,20)}, v = 0$	$24_{(6,19)}, v = 1$	1.607E-04	357	178.4
251 574.351	$27_{(2,26)}, v = 0$	$26_{(2,25)}, v = 1$	3.873E-04	385	179.3
251 577.144	$27_{(1,26)}, v = 0$	$26_{(1,25)}, v = 1$	3.870E-04	495	179.3

Table A.3. Spectroscopic data of the gGg′ ethylene glycol lines displayed in Fig. 4.

frequency (MHz)	Quantum number[a] J_{K_a,K_c}, v(up)	J_{K_a,K_c}, v(low)	$A_{u,l}$ (s^{-1})	g_{up}	E_{up} (K)
217 539.718	$22_{(2,20)}, v = 0$	$21_{(2,19)}, v = 1$	1.495E-04	315	126.6
218 712.336	$22_{(3,20)}, v = 1$	$21_{(3,19)}, v = 0$	1.512E-04	315	126.7
220 249.787	$22_{(2,20)}, v = 1$	$21_{(2,19)}, v = 0$	1.550E-04	405	126.7
229 906.833	$24_{(2,23)}, v = 1$	$23_{(1,22)}, v = 1$	1.013E-04	343	142.7
231 212.070	$24_{(1,23)}, v = 1$	$23_{(1,22)}, v = 0$	1.210E-04	441	142.7
231 366.043	$25_{(1,25)}, v = 0$	$24_{(1,24)}, v = 1$	1.185E-04	357	147.0
231 366.176	$25_{(0,25)}, v = 0$	$24_{(0,24)}, v = 1$	1.184E-04	459	147.0
232 706.108	$25_{(0,25)}, v = 1$	$24_{(1,24)}, v = 1$	1.199E-04	357	147.1
232 706.561	$25_{(1,25)}, v = 1$	$24_{(0,24)}, v = 1$	1.201E-04	459	147.1
233 690.540	$22_{(4,18)}, v = 1$	$21_{(4,17)}, v = 0$	1.118E-04	405	134.2
234 047.938	$25_{(1,25)}, v = 1$	$24_{(1,24)}, v = 0$	1.225E-04	459	147.1
234 048.079	$25_{(0,25)}, v = 1$	$24_{(0,24)}, v = 0$	1.226E-04	357	147.1
234 150.007	$23_{(8,15)}, v = 0$	$22_{(8,14)}, v = 1$	1.039E-04	423	166.1
236 771.321	$23_{(6,17)}, v = 0$	$22_{(6,16)}, v = 1$	1.139E-04	423	153.1
236 845.214	$23_{(7,17)}, v = 1$	$22_{(7,16)}, v = 0$	1.102E-04	423	159.0
236 864.590	$23_{(3,20)}, v = 1$	$22_{(3,19)}, v = 0$	1.058E-04	329	142.4
245 205.575	$25_{(2,23)}, v = 0$	$24_{(3,22)}, v = 0$	1.714E-04	459	160.6
245 215.148	$24_{(7,18)}, v = 0$	$23_{(7,17)}, v = 1$	1.232E-04	441	170.8
245 238.282	$24_{(12,12)}, v = 1$	$23_{(12,11)}, v = 0$	1.016E-04	441	216.4
245 238.282	$24_{(12,13)}, v = 1$	$23_{(12,12)}, v = 0$	1.016E-04	343	216.4
245 424.852	$24_{(11,14)}, v = 1$	$23_{(11,13)}, v = 0$	1.073E-04	343	205.3
245 424.853	$24_{(11,13)}, v = 1$	$23_{(11,12)}, v = 0$	1.073E-04	441	205.3
245 681.514	$24_{(10,15)}, v = 1$	$23_{(10,14)}, v = 0$	1.126E-04	343	195.2
245 681.559	$24_{(10,14)}, v = 1$	$23_{(10,13)}, v = 0$	1.126E-04	441	195.2
245 742.900	$24_{(6,19)}, v = 0$	$23_{(6,18)}, v = 1$	1.280E-04	441	164.8
246 042.955	$24_{(9,16)}, v = 1$	$23_{(9,15)}, v = 0$	1.176E-04	343	186.0
246 044.081	$24_{(9,15)}, v = 1$	$23_{(9,14)}, v = 0$	1.176E-04	441	186.0
250 230.085	$19_{(4,15)}, v = 0$	$18_{(3,15)}, v = 1$	1.043E-04	351	102.1
250 473.822	$25_{(4,22)}, v = 0$	$24_{(4,21)}, v = 1$	1.059E-04	357	166.5

Notes. [(a)] Tunnelling is observed between two equivalent equilibrium configurations and splits each rotational level into two distinct states designated $v = 0$ and $v = 1$ (BD15).

Appendix B: Additional table

Table B.1. Relative abundances.

Component	$\frac{CH_3COOH}{aGg'(CH_2OH)_2}$	$\frac{CH_3COOH}{gGg'(CH_2OH)_2}$	$\frac{aGg'(CH_2OH)_2}{gGg'(CH_2OH)_2}$
8 km s^{-1}	1.8	4.4	2.5
5 km s^{-1}	2.4	5.0	2.3

Notes. The given values have uncertainties of 40%–50%.

Appendix C: Contamination

Figure C.1 shows that the acetic acid emission at 219 016 MHz is partially contaminated by the emission from an unidentified species toward the northwest region from the EGP peak.

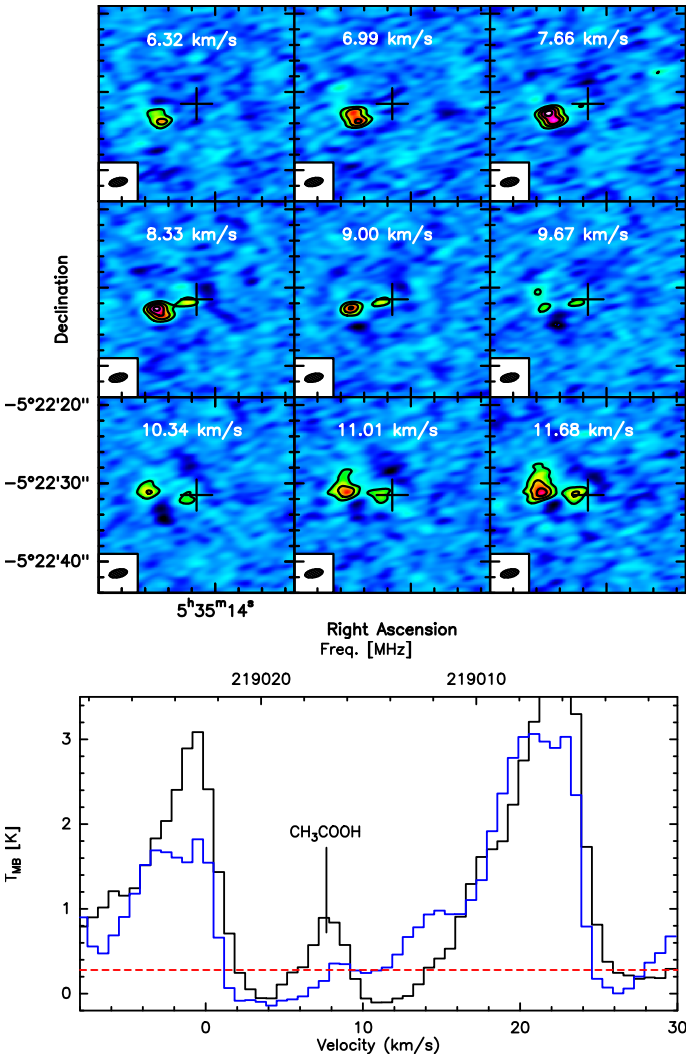

Fig. C.1. *Top Panel*: CH_3COOH channel emission maps at 219 016 MHz. *Bottom Panel*: spectra centred at 219 016 MHz. The black spectrum is taken in direction of the EGP emission peak while the blue one is taken in direction of the northwest clump which contaminates the CH_3COOH emission maps displayed here as well as in Fig. 1. The red dashed line shows the 3σ noise level of the spectrum taken in direction of the northwest clump.

Appendix D: Comparison with the $HCOOCH_3$ emission

Figure D.1 illustrates the fact the distribution of the emission associated with the acetic acid and the ethylene glycol molecules differs from that of typical O-bearing species, such as methyl formate ($HCOOCH_3$) within Orion-KL.

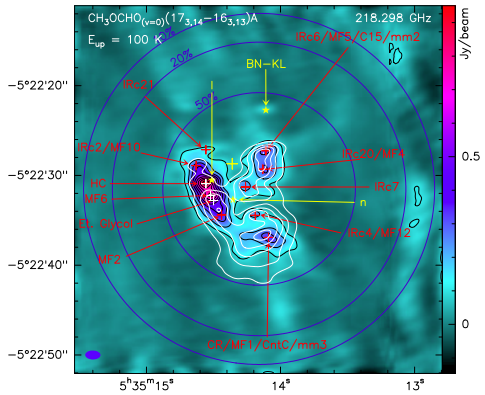

Fig. D.1. Continuum emission at 1.3 mm (color) overlaid with the $HCOOCH_3$ (write contours) emission at 218 298 MHz. Positions of the sources analysed in our Paper I are also given.

Appendix E: HC_3N molecular ring and acetic acid and ethylene glycol emission

The three panels of Fig. E.1 show the HC_3N ring-like structure emission (Wright & Plambeck 2017) overlaid with the emission of acetic acid, aGg′–ethylene glycol and gGg′–ethylene glycol toward the Orion Kleinmann–Low nebula.

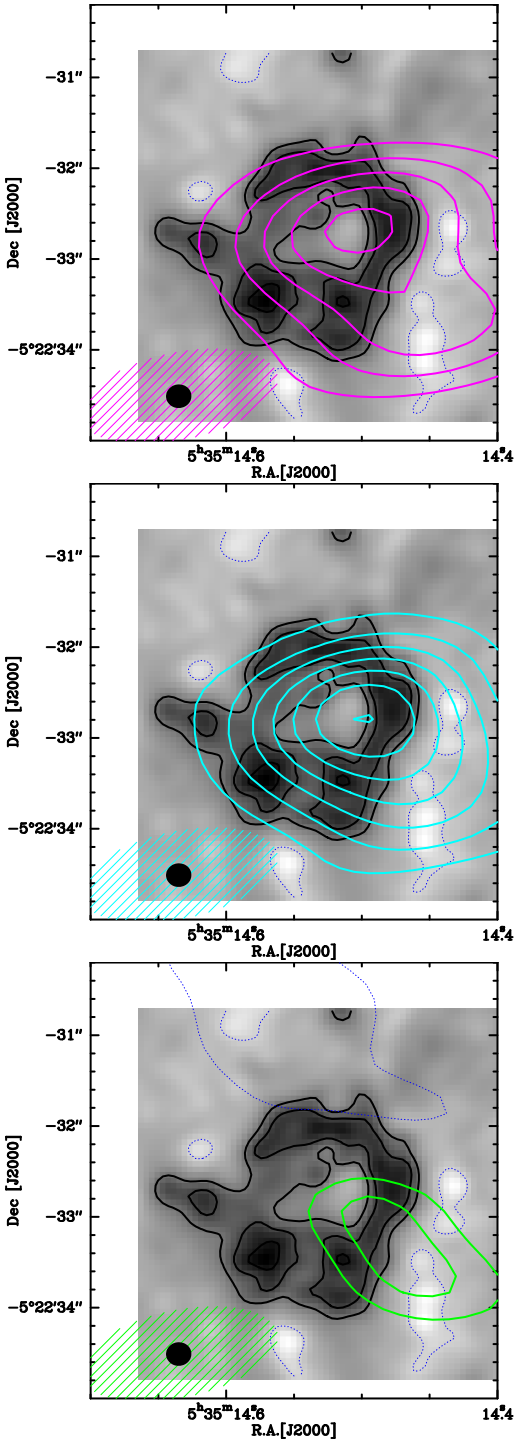

Fig. E.1. ALMA observations of the HC_3N emission at 354.69 GHz (in grey scale, see Wright & Plambeck 2017) overlaid with the emission of acetic acid (purple contours, *top panel*), aGg′–ethylene glycol (cyan contours, *middle panel*) and gGg′–ethylene glycol (green contours, *bottom panel*). The ALMA synthesized beams are shown as the black circles for the HC_3N data (Wright & Plambeck 2017) and as colored ellipses for our data.